Piezoelectric resonator design and analysis from stochastic car vibration using an experimentally validated finite element with viscous-structural damping model

Khazaee, Majid; Rezaniakolaei, Alireza; Rosendahl, Lasse

Published in:
Sustainable Energy Technologies and Assessments

DOI (link to publication from Publisher):
10.1016/j.seta.2022.102228

Publication date:
2022

Document Version
Publisher's PDF, also known as Version of record

Citation for published version (APA):
Khazaee, M., Rezaniakolaei, A., & Rosendahl, L. (2022). Piezoelectric resonator design and analysis from stochastic car vibration using an experimentally validated finite element with viscous-structural damping model. *Sustainable Energy Technologies and Assessments*, *52*(Part C), Article 102228. https://doi.org/10.1016/j.seta.2022.102228

Sustainable Energy Technologies and Assessments 52 (2022) 102228

Contents lists available at ScienceDirect

Sustainable Energy Technologies and Assessments

journal homepage: www.elsevier.com/locate/seta

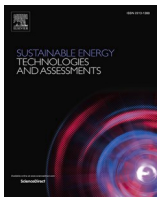

Piezoelectric resonator design and analysis from stochastic car vibration using an experimentally validated finite element with viscous-structural damping model

Majid Khazaee, Alireza Rezania *, Lasse Rosendahl

AAU Energy, Aalborg University, Pontoppidanstræde 111, 9220 Aalborg East, Denmark

ARTICLE INFO

Keywords:
Piezoelectric
Energy harvesting
Finite element
Optimization
Car-vibration

ABSTRACT

Within the Vibration Piezoelectric Energy Harvesting (VPEH) framework, this paper investigates and designs an optimal piezoelectric harvester (PH) under stochastic real-time vibrations using a step-by-step guideline from an electrical and mechanical perspective. A stochastic-excitation high-order-shear-deformation finite element (FE) method, with experimental verifications, analyzed the trapezoid non-uniform piezoelectric resonator under random base vibration. The significance of the contact layer and proper viscous-structural combined damping model is reported for precise power estimation. Based on modal sensitivity, a fast and effective model-updating method for structural modulation is developed. Parametric studies of the optimum load–frequency and natural frequency-geometrical parameters relationships are investigated. Modeling results indicate that ignoring the contact-layer effect will create inaccuracies in the resonant frequency estimation. Besides, a combined viscous-structural damping model is mandatory for proper resonant power estimation. The matched resistance loading is slightly different under stochastic vibration than the harmonic analysis. The presented method is applied on a real-time stochastic vibration, i.e., car vibration. Electrical power of 1.32 mW with density of 495.92 $\mu W/cm^3$ are produced by installing one PH undergoing random excitation from gravity-direction. This power can be enough to power a low-power autonomous wireless vibration sensor demonstrating the VPEH usage in autonomous sensors for future intelligent cars.

Introduction

Vibration piezoelectric energy harvesting (VPEH) is an exciting platform [1] for self-powered sensors due to state-of-the-art electronics' low power consumption and unavoidable everyday experiencing vibration. Piezoelectricity in the VPEH is a mature technology with a relatively high power density and easy to implement toward powering multi-sensors autonomously, such as wind turbine blade for wireless sensor [2], water pump for RF transmitter [3], traffic-induced vibration for wireless sensors [4], and pavement roadways [5]. Classical piezoelectric harvesters (PHs) are cantilevered rectangular beams with embedded piezoelectric layers attaching to a vibration source and undergoing linear transverse vibration [6]. Recent VPEH studies investigate four globally categorized areas, namely material development such as functionally graded materials [7] and self-excited energy harvesters [8], new industrial applications such as journal bearing [9], proposing nonlinear designs for performance improvement in specific applications such as flexible piezoelectric films [10] and piezoelectric beams with stoppers [11], and new modeling techniques such as variable thickness finite element modeling [12]. This study focuses on new industrial applications and modeling and optimization techniques for stochastic-excitation VPEH.

PHs, as the electromechanical Multiphysics structures, have vibration, electrical, and the coupling between these domains, involving structural and electrical PH's characteristics [13]. Practical kinetic sources often induce a complex random signal containing randomness. The real-world random signal excitations may influence the effectiveness and piezoelectric harvester optimization processes, emphasizing the analysis of PHs by the random vibration analysis. A random analysis is necessary if the excitation bandwidth exceeds the harvester power bandwidth, and white noise analysis applies only to substantial bandwidth signals [14]. There were studies associated with the PH random analysis, such as the electrical circuit propositions under random signal [15] and white noise [16], and mechanical modeling, e.g., the single-

* Corresponding author.
E-mail address: alr@energy.aau.dk (A. Rezania).

https://doi.org/10.1016/j.seta.2022.102228
Received 21 October 2021; Received in revised form 15 March 2022; Accepted 14 April 2022
Available online 21 April 2022

degree-of-freedom (SDOF) model, under white noise [17], and Gaussian colored noise [18]. Renaud et al. [19] studied the piezoelectric rectangular unimorph efficiency and optimal power using a lumped simple model under harmonic and random excitations. Yoon et al. [20] employed laboratory nonstationary modulated signals and beam-type models for the time-varying study of a piezoelectric bimorph without tip mass. A bimorph beam with proof mass was studied under real-time rail-induced vibration [21]. These studies investigated rectangular single or double piezoelectric layers with or without tip mass; therefore, the lumped and analytical beam models could be applied. While these models provide straightforward outcomes, they are case-dependent, suitable for rectangular shapes, and need new modeling efforts by changing the boundary conditions or vibration mechanisms. Using SDOF [22], single-mode beam distributed model [23], and single electromechanical element [24] over-simplified the piezoelectric behavior and led to inaccuracies; in addition, they are only applicable to simple uniform piezoelectric geometries [25]. In addition, damping in these studies are pure viscous damping, and the bonding layer effect is often eliminated, while the structural damping and the bonding layer have considerable effects on the PH power generation [26]. Regarding the electromechanical coupling, the excitation frequency can change the optimal piezo-harvester layup [27].

PH structure and electrical optimization toward better power generation is always a key VPEH research area and often involves mechanical and electrical modulations [28]. Genetic algorithm for rectangular unimorph optimization by thickness, width, and resistance load tuning. [29], classical plate laminate finite element (FE) for variable thickness beam optimization [12] and evolutionary algorithm for the multi-modal unimorph beam optimization [30] are examples of numerical mechanical PH optimizations. These optimization studies are rational cost-effective numerical methods for lumped or beam piezoelectric models. Nevertheless, numerical optimization such as genetic algorithms will be costly under an accurate high-order FE modeling as a comprehensive, widely applicable modeling technique. The optimal resistance load (as electrical modulation) and resonant frequency matching (as mechanical modulation) are frequency-dependent, creating issues in finding the accurate resonant frequency and optimal resistance load. This issue under random broadband vibration has not received enough attention.

To sum up, to fill the gap in the literature, this study aims to accurately model a wide range of the initiative PH design under a practical random vibration case, explore the effect of the bonding layer and structural damping, and propose a fast method for electrical and mechanical modulations under random excitation considering electromechanical coupling. A powerful high-order shear element finite element (FE) method considering bonding layer and structural damping is elaborated under the random vibration input. The presented FE model is different from classical plate theory FE [25], where shear stresses are ignored, and the presented FE will have higher accuracy and apply to various PH configurations. Experimental verification for clarifying the structural damping contribution in the FE model is reported as a novel modeling improvement. Power generation under wideband random signal is investigated for different dominant frequencies and bandwidths. While single- and double-layer piezoelectric harvesters are primarily studied like the previous mechanical modulation studies, the FE method can be modified for multi-piezoelectric layers. The trapezoid geometry is selected instead of the typical rectangular geometry in the literature; moreover, the FE method accommodates any geometries provided the mesh section is done. Toward the resonator design and for less computational effort in the high-order element FE method, the classical global sensitivity method based on the modal parameters is applied for the PH optimization. This optimization method is model-based, applicable to any design parameter, and is fast convergence with low iterations, which can be expected to have better performance than the random-based numerical optimization algorithms. To elaborate on the natural frequency and optimum resistance sensitivity analysis, the natural frequency and optimum resistance sensitivities under random signals are analyzed. Our findings might be crucial for developing, analyzing, and optimizing piezoelectric energy harvesters effectively and straightforwardly.

As the random signal case study, car vibration is selected because there is a high potential for the autonomous onboard in smart cars sensors [31], on the other hand, car unavoidably experiences vibration [5,32] because of road unevenness, suspension system, engine combustion, and mechanical components' motion (rotation). This vibration energy is often wasted; it can be stored for several self-powered sensors, eliminating the wiring or battery exchange. A non-uniform trapezoid bimorph with a tip mass, which has a unique capability for frequency matching, is proposed for car VPEH. The energy-harvesting box with three directional energy-harvesting beams is attached to the car's body at points where an autonomous sensor is required, as shown in Fig. 1. The trapezoid substrate's geometry and added tip mass are considered because this configuration will lower the PH's natural frequency and increase the power generation.

This study is presented as follows. Section 2 presents the methodology for simulating and designing a piezoelectric harvester beam under stochastic vibration, including the finite element (FE) modeling and the optimization (structural and electrical modulations). The mesh sensitivity analysis, experimental verification, and contact layer effect are studied in this section. Section 3 presents the results from the investigation and designing the energy harvester from stochastic car vibration in an analogous way to the methodology. Finally, section 4 presents the piezoelectric harvesters' power from the real-time stochastic vibration data and the effect of stochastic vibration characteristics on the power output. Concluding remarks and future works are presented in section 5.

Methodology

Finite element model of piezoelectric devices

Cantilevered piezoelectric beams are among the most popular harvesters. These beams can have one piezoelectric layer (unimorph) or two layers (bimorph). Bimorph harvesters are more popular because they provide one extra piezoelectric layer without design difficulties. The harvester beam can have an added tip mass to reduce the beam's natural frequency and increase output voltage by creating extra mechanical strain. A bimorph beam is investigated in this research, as shown in Fig. 2; nevertheless, the FE model can be applied on single or higher number piezoelectric layers. An adhesive contact layer attaches the piezoelectric layer and substrate shim. This work uses the finite element (FE) method, as it has been demonstrated that the FE model is the most accurate and comprehensive for all designs [25]. In the FE method, the beam domain is divided into finite (small) elements, and the plate-theory equations of motions are derived for each element. The general FE method, previously derived by authors [19], will be employed in this study. The plate theory of Carrera's advanced plate theory with First Shear Deformation Theory (FSDT) is considered because, according to Ref. [19], ignoring shear stresses leads to inaccurate natural frequency estimation.

Fig. 2 shows one piezoelectric harvester (PH), a trapezoid substrate shim, and two rectangular piezoelectric patches. The rectangular shape of piezoelectric patches will ease the use of available commercial piezoelectric layers, while the trapezoid substrate shim will provide the opportunity for easy resonant-frequency matching. The elements in the FE method, as shown in Fig. 2, are 4-node elements, and each element has 24 Degrees of Freedom (DOFs). The PH's base excitation is a random signal indicated by $\ddot{a}_B(t)$ with the power spectral density (PSD) $\Phi_{BB}(\omega)$. The transfer function $H(\omega)$ relates the input acceleration to the output voltage. $V_p(t)$ denotes the output voltage with the PSD $\Phi_{VV}(\omega)$. The FE model aims to obtain the average voltage and power in connection with resistance load R under the random vibration input.

According to the extended Hamilton's principle, the variation of

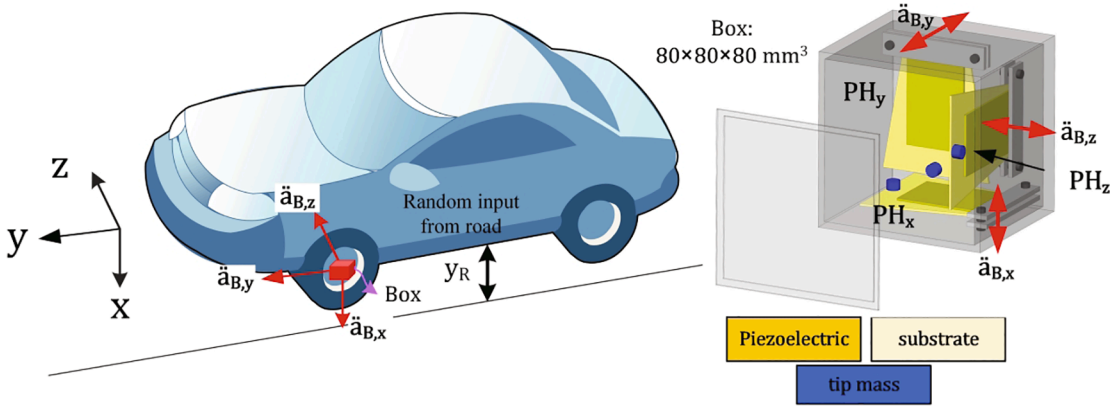

Fig. 1. A moving car and the energy-harvesting box comprising three directional non-uniform trapezoid piezoelectric harvesters.

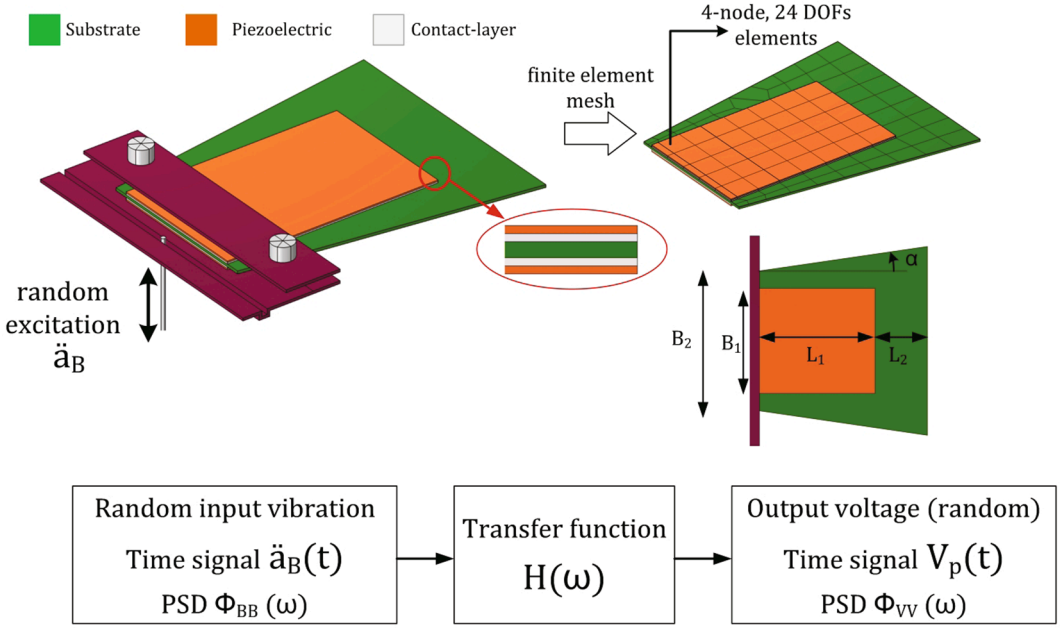

Fig. 2. Piezoelectric bimorph as vibrating energy harvester subjected to a random vibration.

total energy from 0 to t_0 along all feasible paths is zero, Eq. (1.a) [25]. An integral-based equation over the volume is obtained by inserting the definitions of kinetic and potential energy for non-piezoelectric and piezoelectric domains and external mechanical forces, as expressed by Eq. (1.b),

$$\delta\int_0^{t_0}[(K.E.-P.E.+W_{el})+W_E]dt=0 \tag{1a}$$

$K.E.$ = kineticenergy, $P.E.$ = potential energy, W_{el} = electric energy, W_E = external mechanical.

$$\delta\int_0^{t_0}\left[\overbrace{\iiint\rho\delta\dot{\boldsymbol{r}}^t\dot{\boldsymbol{r}}\mathrm{dV}}^{K.E.}-\overbrace{\iiint\rho\delta\boldsymbol{\varepsilon}^t\boldsymbol{\sigma}\mathrm{dV}+\iiint\delta\boldsymbol{\varepsilon}^t\boldsymbol{e}^t\mathbf{E}\mathrm{dV}_p}^{P.E.}+\overbrace{\iiint\delta\boldsymbol{E}^t\boldsymbol{e}\boldsymbol{\varepsilon}\mathrm{dV}_p+\iiint\delta\boldsymbol{E}^t\boldsymbol{D}\mathrm{dV}_p}^{W_{el}}+\overbrace{\delta\boldsymbol{r}\boldsymbol{f}_E}^{W_E}dt\right]=0 \tag{1b}$$

ρ: density $\boldsymbol{r}$: mechanical displacement field $\boldsymbol{\varepsilon}$: strain $\boldsymbol{\sigma}$: stress $\boldsymbol{f}_E$: external force.

$\boldsymbol{e}$: piezoelectric factor $\mathbf{E}$: electric field $\boldsymbol{D}$: electric displacement field.

A matrix-form set of differential equations is required for each element in the mesh in Fig. 2. A high order shear element (TSDT) is assumed in this FE method, as shown in Fig. 3. The overall equation, Eq. (1.b), can be converted to element-wise equations for each discretized element. The element differential equations for a piezoelectric beam connected to a resistance load R are given by:

$$\begin{gathered}[m^e]\{\ddot{\chi}^e\}+\left[c_a^e\right]\{\dot{\chi}^e\}+\left(\left[k_{qq}^e\right]+j\left[c_s^e\right]\right)\{\chi^e\}-\left[k_{q\phi}^e\right]v_e=\boldsymbol{f}_E\\ \left[k_{q\phi}^e\right]^t\{\ddot{\chi}^e\}+\frac{\dot{v}_e}{R}+k_{\phi\phi}^e\dot{v}_e=0\end{gathered} \tag{2}$$

wherein $\{\chi^e\}\in\mathbb{R}^{6\times1}$ is the mechanical degrees of freedom for each element, $v_e\in\mathbb{R}$ is the voltage difference between electrodes at each element, $[m^e]\in\mathbb{R}^{6\times6}$ is the element mass matrix, $\left[k_{qq}^e\right]\in\mathbb{R}^{6\times6}$ is the element stiffness matrix, $\left[k_{q\phi}^e\right]\in\mathbb{R}^{6\times1}$ is the element electromechanical coupling matrix, $\left[c_a^e\right]\in\mathbb{R}^{6\times6}$ is the element viscous-damping matrix, and $\left[c_s^e\right]\in\mathbb{R}^{6\times6}$ is the element structural-damping matrix. The definitions for these element matrixes can be found in Ref. [25].

After the element derivations of matrices, by assembling the element matrices, the global FE differential equations can be obtained, as given

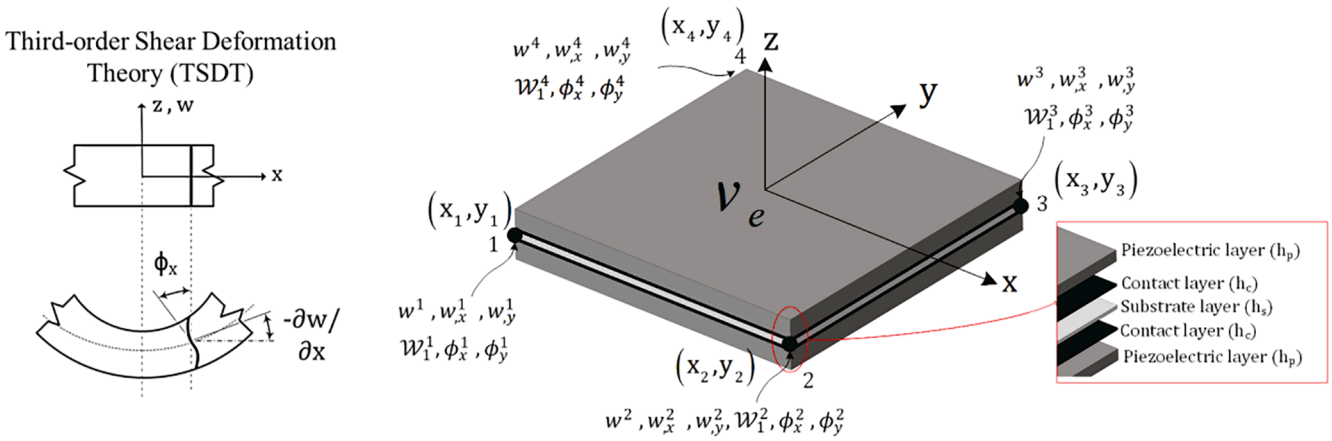

Fig. 3. Discrete quad element using Third-order Shear Deformation Theory and its degrees of freedom.

by:

$$\begin{aligned}[M]\ddot{\underline{\chi}}(t)+[C_a]\dot{\underline{\chi}}(t)+\left(\left[K_{qq}\right]+j[C_s]\right)\underline{\chi}(t)-\left[\widetilde{K}_{q\phi}\right]V_p(t)=\underline{F}(t)\\ \left[\widetilde{K}_{q\phi}\right]^t\dot{\underline{\chi}}(t)+V_p(t)\Big/R+K_{\phi\phi}\dot{V}_p(t)=0\end{aligned}\tag{3}$$

In this FE formulation, the viscous and structural damping mechanisms are separately considered by $[C_a]$ and $[C_s]$ matrices, respectively. The viscous damping matrix $[C_a]$ is proportional damping and represented by $\beta[M]$. The structural damping matrix is also proportional and is represented by $[C_s]=\gamma\left[K_{qq}\right]$. If one obtains the structural (η_n) and viscous (ζ_n) damping coefficients from the experiments, β, and γ can be calculated by [34]:

$$\begin{aligned}\beta&=2\zeta_n\omega_n\\ \gamma&=\eta_n\end{aligned}\tag{4}$$

If there is a base vibration of $\ddot{a}_B(t)=\ddot{A}_B(\omega)e^{j\omega t}$, then the input excitation force is due to the inertial load, which $F_-(t)=m_{\text{eff}}a_B\omega^2e^{j\omega t}\{\mathscr{T}\}$ expresses. In this case, the voltage output is $V_p(t)=\overline{V}_{p,\omega}e^{j\omega t}$, which is related to the base vibration by $\overline{V}_{p,\omega}=H(\omega)\ddot{A}_B(\omega)$ (H is the transfer function). The transfer function of voltage to the input vibration $H(\omega)$ is obtained from Eq. (3) and can be expressed by:

$$H(\omega)=\frac{V_{p,\omega}}{\ddot{A}_B(\omega)}=m_{\text{eff}}\frac{j\omega\left(1/R+j\omega K_{\phi\phi}\right)^{-1}\left[\widetilde{K}_{q\phi}\right]^t\{\mathscr{T}\}}{\left(\left(-\omega^2+j\omega\beta\right)[M]+(1+j\gamma)\left[K_{qq}\right]+j\omega\left(1/R+j\omega K_{\phi\phi}\right)^{-1}\left[\widetilde{K}_{q\phi}\right]\left[\widetilde{K}_{q\phi}\right]^t\right)}\tag{5}$$

$\{\mathscr{T}\}$ is the vector containing the applying force degrees of freedom.

The resonant frequency ω_r of the transfer function $H(\omega)$ is a function of natural frequency, damping coefficients, and the electromechanically piezoelectric coupling coefficients [13], e.g., $\omega_r=\sqrt{\omega_n^2+f\left(\left[\widetilde{K}_{q\phi}\right],K_{\phi\phi},\omega,R,\beta,\gamma\right)}$, where the coupling function f is nonlinear. The resonant frequency dependency function f has been previously investigated by analytical model for single-mode viscous damping in Ref. [13]; while using the matrix formulation, this dependency shall be investigated numerically.

For the harmonic excitation case, the power output normalized per square acceleration can be obtained by $P(\omega)=\frac{1}{R}\left(\frac{V_{p,\omega}}{\ddot{A}_B(\omega)}\right)^2=\frac{(H(\omega))^2}{R}$. Therefore, the optimum resistance load is frequency-dependent and depends on the material properties and geometries.

For the stochastic vibration case, the harvester base excitation, $\ddot{a}_B(\omega)$, is a stationary random vibration, and its power spectral density is $\Phi_{BB}(\omega)$. The voltage PSD then can be obtained by.

$$\Phi_{VV}(\omega)=|H(\omega)|^2\Phi_{BB}(\omega)\tag{6}$$

In the random vibration, then it is possible to calculate the average harvested power by:

$$E[P(t)]=\frac{E\left[V_p^2(t)\right]}{R}=\frac{1}{R}\left(\int_{-\infty}^{\infty}|H(\omega)|^2\Phi_{BB}(\omega)\right)\tag{7}$$

wherein $E[\cdots]$ is the average. The above integration shall be calculated numerically.

Mesh sensitivity analysis

The number of elements or divisions in the FE mesh affects the FE results. Thus, mesh analysis is essential prior to further investigations by this FE method. The FE numerically models a bimorph sample for mesh sensitivity analysis. The bimorph sample consists of two oppositely poled PZT-5H layers embracing a brass substrate, representing a series

Table 1
Material properties of bimorph piezoelectric energy harvester (Q220-H4BR-2513YB) [35].

Properties	Values
Piezoelectric stiffness at the constant field, c_{11}^E, GPa	66.7
Piezoelectric density, ρ_p, kg/m^3	7870
Electromechanical coupling coefficient, e_{31}, C/m^2	−35.5
Piezoelectric layer thickness (each), t, mm	0.19
Piezoelectric permittivity constant, $\bar{\varepsilon}_{33}$, F/m	3800×ε_0
Substrate Young's modulus, Y_s, GPa	100
Substrate thickness, h, mm	0.13
Substrate density, kg/m^3	8300
Piezoelectric beam length, l, mm	57.2
Piezoelectric beam width, b, mm	31.8
Bonding layer thickness, mm	0.02

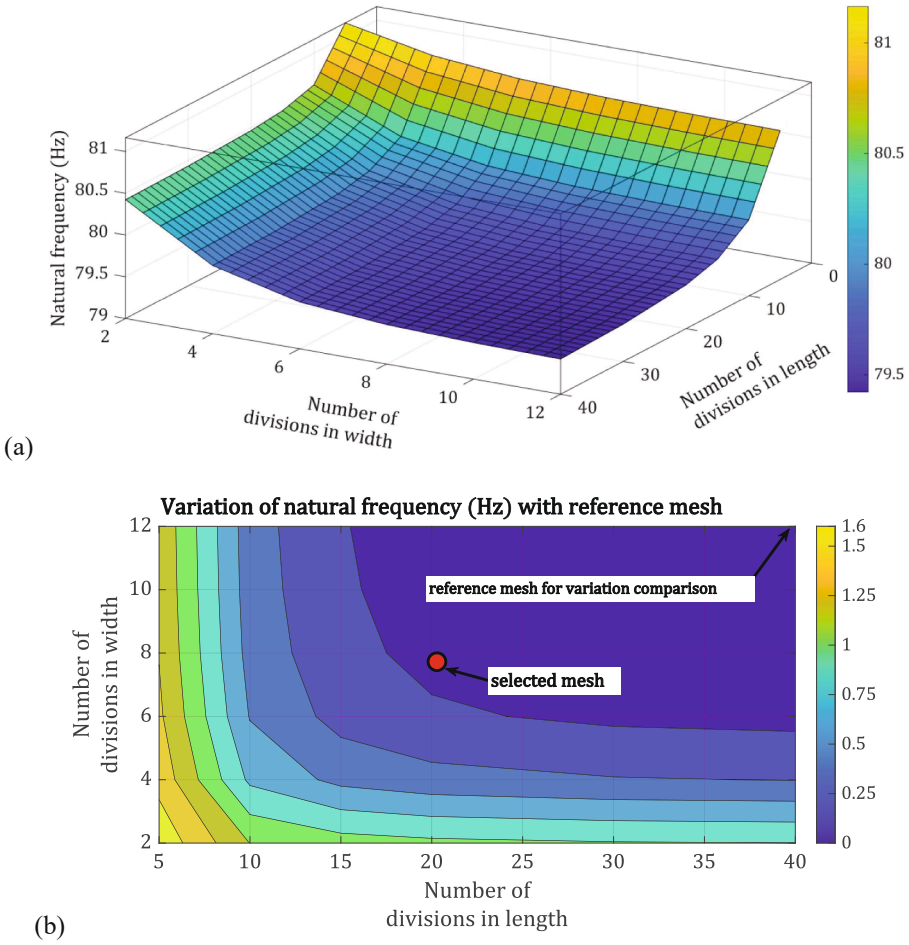

Fig. 4. Mesh study for the bimorph sample (Q220-H4BR-2513YB), (a) the natural frequency, and (b) the natural frequency variation, as a function of divisions in length and width.

connection between the piezoelectric elements. The geometric and material properties of these samples are presented in Table 1.

Mesh size is characterized by the division number in length N_l and width N_w. The natural frequency is investigated in mesh size from 10 elements ($N_l = 5$ and $N_w = 2$) to 480 elements ($N_l = 40$ and $N_w = 12$), see Fig. 4 (a). As expected, the natural frequency converges to a more accurate value by increasing the element numbers; here, the natural frequency reduces from 81.16 with 10-element divisions to 79.42 with 480-element divisions. In addition, the natural frequency value becomes less sensitive to the element numbers when mesh numbers are sufficiently

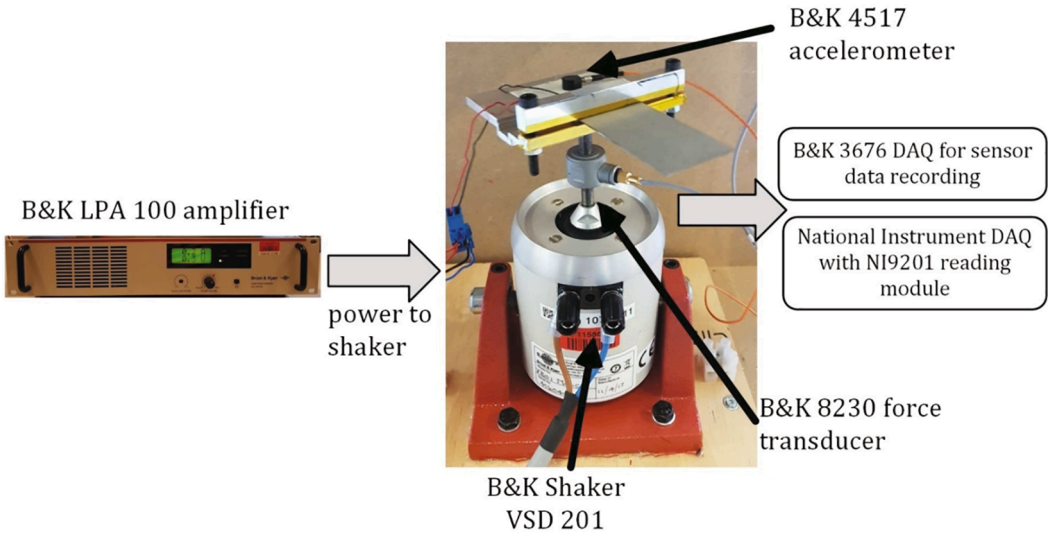

Fig. 5. Experimental setup for model verification.

large. However, this accuracy comes with a price of computation time, which dramatically increases for large element divisions. For instance, the computation time in a laptop (CPU: Intel(R) Core(TM) i7-6600U 2.81 GHz and RAM: 20 GB) for 10, 160, and 480 elements are 3.59, 11.87, and 61.74 s, respectively. Therefore, mesh size is a trade-off between accuracy and computation time.

Fig. 4 (b) shows the natural frequency variation versus the element divisions with the reference mesh (a 480-element mesh). An area with $N_l \geq 20$ and $N_w \geq 8$ gives a natural frequency with<0.25 Hz variation, e.g., <0.3%. This 160-element mesh is selected, with 20 divisions in length and 8 divisions in width, as further mesh refinement does not change the FE results substantially.

Experimental verification of the FE model

The bimorph sample (Q220-H4BR-2513YB) from Piezo.com [35] is subjected to experimental tests and FE analysis for experimental verification. The bimorph in the clamp-free boundary condition, as shown in Fig. 5, is subjected to the base excitation from a vibrating shaker. A force transducer and an accelerometer measure the input force and acceleration during the excitation. In addition, the generated voltage from the piezoelectric harvester is measured by the National Instrument (NI) Data Acquisition (DAQ) system.

A proper damping model is essential for the proper harvester performance modeling. Using the damping determination method in Ref. [13], the mechanical damping coefficient, which contains viscous and structural damping mechanisms, is calculated based on transient harmonic response and is 8.04%. According to Ref. [36], if the total damping contribution is viscous damping, then the output resonant power is considerably lower than a half-half viscous-structural damping contribution. The proper determination of viscous and structural damping contributions is a complex process. Khazaee et al. [26] presented a study on the experimental determination of the viscous and structural damping contributions. According to Ref. [26], the viscous and structural damping contributions for a thin-layer piezoelectric harvester are considered 64% and 36%, respectively. These contributions are also employed in this FE model.

Table 2 compares the first mode natural frequency at short-circuiting (R = 0) and R = 30kΩ load resistance cases. The short-circuiting natural frequency is compared with the datasheet result, while the load resonant frequency is compared with the experimental data. In both cases, the difference between the FE model and the validation sources is<2%, which is a reasonable error. Moreover, the FE model can capture the effect of load on the natural frequency of energy harvester. Ref. [28] shows more details about the dependence of natural frequency on electromechanical coupling properties.

The output voltage and power are compared with the experimental data in Fig. 6 with two damping models, pure viscous and combined viscous-structural damping models. There is a good agreement between the experiment and the FE model with the viscous-structural damping model, while the pure viscous damping model underestimates the output power. This comparison emphasizes that a proper damping model is a combined viscous and structural damping model. This conclusion agrees with the observations about the experimental results on the damping energy sources [26,37,38]. Damping sources in a cantilevered bender comprise air resistance force, clamping energy dissipation, and internal energy dissipation [39]. These damping sources have different energy dissipation mechanisms, so a combined viscous-structural damping model is required for an accurate damping model. Cooley et al. [40] also used a numerical example to emphasize the importance of a combined damping model.

Table 2
The comparison of structural response between FE model, experiment, and datasheet.

Method	FE	Experiment	Datasheet [35]	Difference
Short-circuit natural frequency,$\omega_{n,R=0}$	79.57	–	78	2.0%
Resonant frequency (Hz) with R = 30 kΩ,$\omega_{n,R}$	82.75	84	–	1.5%

The FE model's output voltage and power agree with the resonance and off-resonance frequencies experiments, as shown in Fig. 6 (a) and (b). As shown in Table 2, the experimental resonant frequency is 1.5% higher than the FE resonant frequency. This frequency shift is also visible in Fig. 6 (a). Since the output voltage (and power) is highly resonant-frequency sensitive, the frequency shift causes more variation around the resonance. However, the peak resonant power and voltage agree between the experimental and FE modeling. Thus, the FE model delivers reasonable power estimations. In addition, this comparison shows that the FE model can also simulate suitably the PH's electrical output performance with resistive load. Therefore, this FE model will be used for the random excitation analysis.

Effect of contact layer in the FE model

The modeling techniques for PH simulation often ignore the contact layer role because of its small thickness. However, Khazaee et al. [26] experimentally demonstrated that the bonding layer changes the harvester's vibration characteristics and substantially affects the power output. Thus, here, for illustrating the bonding layer effect, the harvester's performance is analyzed by two different bonding layer thicknesses, i.e., 1 μm and 20 μm (the manufactured thickness). Table 3 compares the FE model's output power and fundamental natural frequency when the contact layer's thickness is 1 μm (intentionally considered less than the actual value) and 20 μm. According to Table 3, when the contact layer is 1 μm, the FE resonant frequency underestimates the resonant frequency. The output power with an actual contact layer thickness (20 μm) is lower than the 1 μm-thickness bonding layer. The thickness of the bonding layer will increase the harvesting bending stiffness leading to minor bending deformation. This comparison shows that even contact layers of 0.02 mm thickness can lead to inaccuracies in the modeling. Therefore, it is necessary to consider the bonding layer.

Design of piezoelectric harvesting device

This subsection provides a resonator piezoelectric harvester design for external stochastic vibration. The first step deals with vibration analysis of the external stochastic source and calculating the power spectral density and dominant frequency. Then, the optimization process is carried out for resonance maximum power generation. In the PH design, the harvester will generate maximum power when it vibrates at a frequency close to the beam's natural frequency [6] and is connected to an optimum electrical load that matches the beam's internal resistance [13].

Thus, two modulations are required, one structural or mechanical modulation and one electrical modulation. Since the resonant frequency depends on the electrical load, these two modulations are coupled. One solution can be to perform the structural modulation by considering the electromechanical coupling effect and then carry out the electrical modulation. Selecting the beam geometry for resonant frequency matching is an optimization process, which will be solved through a sensitivity-based updating process. The frequency matching process requires that the optimization parameters be updated systematically; a sensitivity-based optimization will be used with different geometry configuration parameters for fast convergence. The electrical modulation is also performed based on entirely random vibration analysis.

Fig. 7 presents the flowchart for this optimization investigation, with four steps, namely, 1. source analysis, 2. natural frequency sensitivity, 3. structural modulation, and 4. electrical modulation. These four steps are discussed as follows.

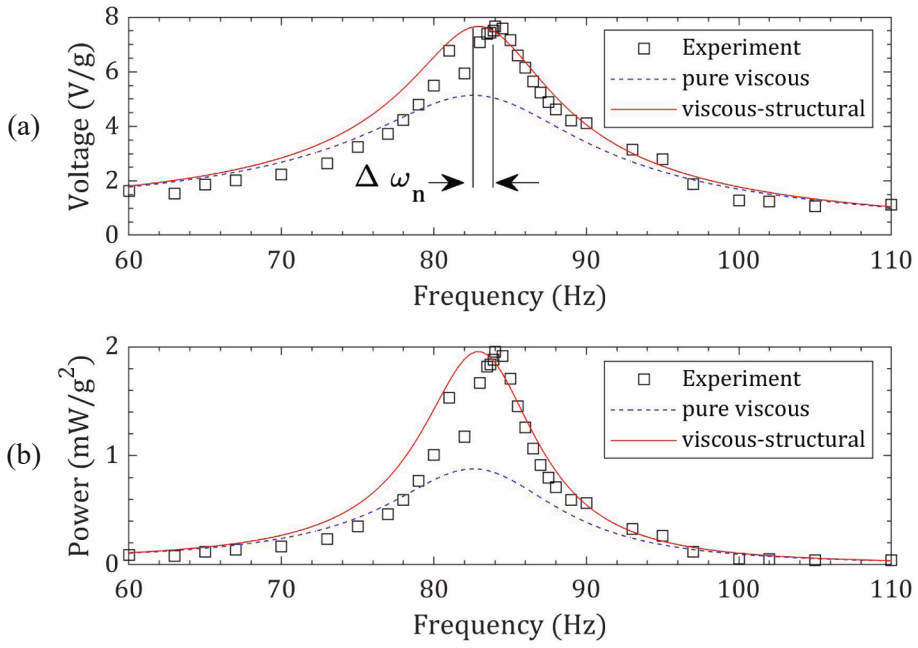

Fig. 6. Comparison of the electrical response output between the FE model and experiments, (a) voltage and (b) power frequency response functions, considering two different damping models (pure viscous and viscous-structural models).

Table 3
Comparison of FE resonant frequency and power output with 1 μm-thickness and 20 μm-thickness contact-layer modeling.

Method	Fundamental natural frequency	Output resonant power
FE model with 1 μm-thickness contact-layer	72.58 Hz	2.25 mW
FE model with 20 μm-thickness contact-layer (actual thickness)	79.57 Hz	1.95 mW
Difference	6.99 Hz	0.32 mW

Step 1: source analysis

The vibration source is a stochastic vibration source. The PSD of the harvester's base excitation, $\Phi_{BB}(\omega)$, can be obtained in two ways. The first way is the experimental measurements of the car vibration at the harvester's installation location. The second way is to estimate the car vibration's PSD from the road's PSD and the car's dynamic model [41,42]. The first way is taken in this study, as experimental data are more realistic and do not require the car dynamic model. $\Phi_{BB}(\omega)$ is a measured sequence; however, since the input acceleration is random, then the distribution of this variable can be estimated by the Gaussian normal distribution. Thus, the PSD of the measured acceleration from a car is:

$$\Phi_{BB}(\omega) \approx \frac{Y_0}{\sigma\sqrt{2\pi}} e^{-\frac{1}{2}\left(\frac{\omega-\Omega}{\sigma}\right)^2} \tag{8}$$

wherein Ω and σ are the dominant frequency and the standard deviation of the PSD of the measured acceleration, and Y_0 is the peak amplitude of the signal.

Step 2: natural frequency sensitivity

The general eigenvalue problem can be written by:

$$[K_{qq}]\Phi_j = \omega_{n,j}^2[M]\Phi_j \tag{9}$$

where it is considered that the eigenvector is mass-orthogonalized, i.e., $\Phi_k^T[M]\Phi_j = \delta_{jk}$.

By differentiating eigenvalue in Eq. (9) concerning the design variable Θ_i, the eigen-sensitivities can be extracted by [43].

$$\frac{\partial\omega_{n,j}}{\partial\Theta_i} = \frac{1}{2\omega_{n,j}}\Phi_j^T\left(\frac{\partial[K_{qq}]}{\partial\Theta_i} - \omega_{n,j}^2\frac{\partial[M]}{\partial\Theta_i}\right)\Phi_j \tag{10}$$

Since natural frequencies have global nature, their sensitivity terms include only the derivates of stiffness and mass matrices concerning the design variables [43], which will make the gradient computation faster than iterative eigenvalue problem-solving.

Step 3: structural modulation

For the mechanical modulation, the product of $|H(\omega)|^2 e^{-\frac{1}{2}\left(\frac{\omega-\Omega}{\sigma}\right)^2}$ should be maximum, and since the Gaussian distribution's maximum occurs at $\omega = \Omega$, $|H(\omega=\Omega)|^2$ is to be maximized. One common practice is to match the natural frequency of the energy harvester, i.e., $\omega_{\mathrm{n,coupled}}$ to Ω.

Generally, let consider that the optimization problem is to update the design variables of $\widehat{\Theta} = \{\Theta_1, \cdots, \Theta_i, \cdots, \Theta_I\} \in \mathbb{R}^I$ to match the harvester's fundamental natural frequency to a targeted value determined from the external vibration source. A cost function is defined by.

$$\epsilon(\widehat{\Theta}) = \left(\omega_{\mathrm{n,coupled}} - \Omega\right)^2 \tag{11}$$

where $\omega_{\mathrm{n,coupled}}$ is the natural frequency with electromechanical coupling effect. $\omega_{\mathrm{n,coupled}}$ is the finite element natural frequency. Starting from a design parameter set $\widehat{\Theta}_N$, the step variation $\Delta\widehat{\Theta}_N$ is calculated by the first-order Taylor series approximation, as expressed by,

$$\widehat{\Theta}_{N+1} = \widehat{\Theta}_N + \frac{\epsilon(\widehat{\Theta}_N)}{\frac{\partial\omega_{\mathrm{n,N}}}{\partial\widehat{\Theta}_N}} \tag{12}$$

where $\frac{\partial\omega_{\mathrm{n,N}}}{\partial\widehat{\Theta}_N}$, natural frequency sensitivity is calculated in step 2.

The sensitivity-based updating process continues until the error function $\epsilon(\widehat{\Theta})$ is below a user-defined threshold.

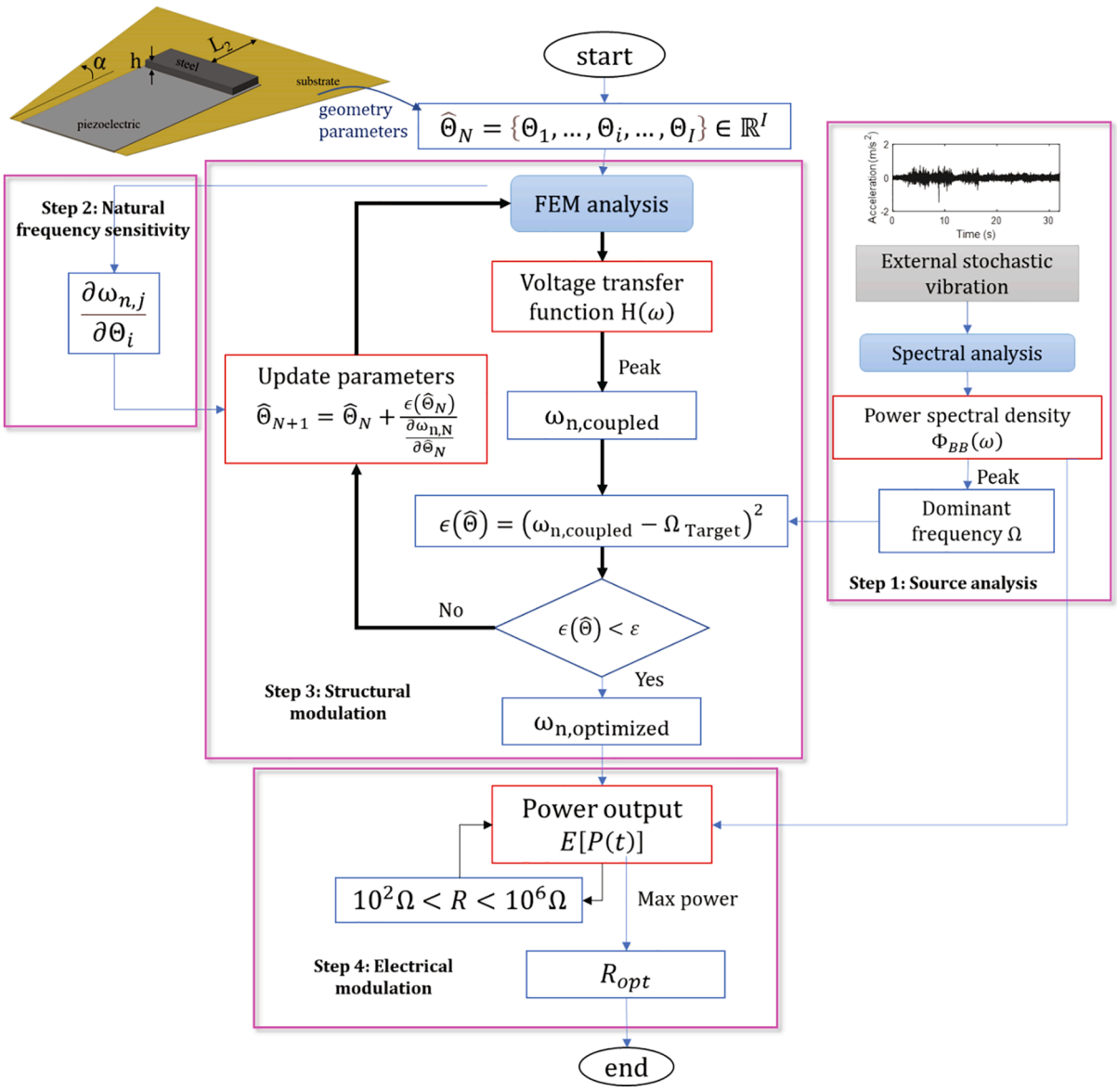

Fig. 7. The flowchart for designing the piezoelectric harvesting device for stochastic vibration excitation.

Step 4: electrical modulation

The optimal resistance load for maximum power generation shall be obtained for the electrical modulation. Inserting this Gaussian distribution of the measured acceleration into Eq. (7), the average power is given by:

$$E[P(t)] \approx \frac{Y_0}{R\sigma\sqrt{2\pi}} \left(\int_{-\infty}^{\infty} |H(\omega)|^2 e^{-\frac{1}{2}\left(\frac{\omega-\Omega}{\sigma}\right)^2} d\omega \right) \cong \frac{Y_0}{R\sigma\sqrt{2\pi}} \left(\int_{\Omega-3\sigma}^{\Omega+3\sigma} |H(\omega)|^2 e^{-\frac{1}{2}\left(\frac{\omega-\Omega}{\sigma}\right)^2} d\omega \right) \quad (13)$$

In Eq. (13), the integral bands are replaced with -3σ and 3σ, as 99.7% of the Gaussian values lie within this interval. The integration in Eq.(13) shall be numerically handled as this integral's analytical solution is unknown. In practice, the trapezoid method is employed for this numerical integral with a $d\omega \approx 0.05$ Hz.

For a single harmonic excitation with $Y(t) = \sqrt{Y_0} e^{j\overline{\Omega}t}$ input excitation, the steady-state peak power can be obtained by $|P| = Y_0 |H(\overline{\Omega})|^2 / R$. For maximum power design, the harvester's resonant frequency is matched, e.g., $\omega_r = \overline{\Omega}$ (structural modulation), and the peak of the transfer function is $|H(\overline{\Omega})|$ maximized versus R (electrical modulation).

In other words, in single harmonic excitation, the transfer function's local peak is of interest and, therefore, a sensitive link between ω_r and R is expected because R changes the ω_r.

On the other hand, for stochastic vibration excitation, the average power involves the integration over a frequency range; therefore, there is a global behavior of the power over a range of frequencies rather than

single resonant power. Analytically, the optimum load cannot be calculated from Eq.(13) because the integration involves the voltage output from all the frequencies. However, as the random input vibration is maximum at $\omega = \Omega$, the resonant power contributes most to the total power. Therefore, the optimum load from a random vibration can be expected to be close to the optimum resonant resistance but not necessarily equal to the optimum resonant resistance. This research question will be examined for the stochastic vibration case.

Results: Piezoelectric harvester design for car vibration harvesting

This section presents the case study results of designing and power optimization in the piezoelectric harvester for stochastic car vibration. Initially, a general harvester is considered, which the material properties are identical to the FE experimental verification example. Then the step-by-step analysis of the design methodology flowchart in Fig. 7 is taken.

General harvester's configuration

Piezoelectric harvesters are available in different geometries, and therefore, the optimization can be performed for any combination of these geometric parameters, such as length or thickness. First, a commercial piezoelectric harvester that the FE model is validated using this sample (Q220-H4BR-2513YB) is selected for narrowing down optimization factors. This sample has PZT-5H as piezoelectric material, which previously showed its privilege for car energy harvesting applications [24]. Then, a benchmark geometry is formed for the optimization process by adding tip mass and trapezoid substrate geometries, as shown in Fig. 8. Then, by tuning the sample length L_2, tip mass M_t (tip mass height h), and tapering angle α, the harvester's fundamental natural frequency matches dominant frequencies for each direction. The optimization parameters are demonstrated in the harvester FE model in Fig. 2. From the mesh study for the optimization example in Figure S1 (supplementary data), a 30 × 15-element mesh is used in this example.

Step 1: Source Analysis, a real-time car stochastic vibration

There are two approaches for car vibration estimation: numerical simulation and experimental measurements. Accurate and realistic simulations require a complex multi-degree-of-freedom model, computationally demanding. Moreover, smoothening the signal may provide numerical stability [44], while this smoothing may misrepresent the actual car vibration signal. Thus, the experimental measurement method is used in this study.

The experimental vibration data are retrieved from the practical vibration database [45]. The car understudy is Renault Clio, an accelerometer placed on the frame close to the wheel and a data acquisition system. Acceleration data has been recorded for 30 s in three directions with a sampling rate of 20000 Hz. Fig. 9 (a) shows the acceleration signals in three directions when the car moves on an urban road. The X-axis is toward the global gravity. Because the road unevenness is not deterministic, the car vibration is random. Vibration frequency plays an essential role in harvester design in energy harvesting applications. Therefore, the PH structural design needs the power spectral density (PSD). The PSDs are calculated using the Fast Fourier Transform and shown in Fig. 9 (b). The acceleration in the gravity is considerably higher than forwarding and lateral directions, as can be observed from the time and PSD signals.

Since the car vibration is random, the Gaussian normal distributions (see Eq. (8)) for the PSDs are plotted in Fig. 9 (b). The parameters for these Gaussian normal distributions can be found in Table S1 (supplementary data). The PSDs in different axes show that the dominant frequencies for different directions differ. For example, while the dominant frequency on the X-axis is the smallest with $\Omega_x = 14.1$ Hz, the dominant frequencies are $\Omega_y = 65.0$ and $\Omega_z = 63.4$ in the Y and Z directions, respectively.

Step 2: Sensitivity of natural frequency to design parameters

The sensitivity is calculated numerically, as the analytical is not solvable. For numeric sensitivity, the FE mesh element size becomes essential. So, a sensitivity analysis was performed for a fine mesh with 434 elements and a coarse mesh with 60 elements, and the sensitivity was, on average, 30% different. Therefore, a fine mesh is employed even though the computation time becomes high.

Fig. 10 (a) shows the natural frequency ratio versus tip mass ratio for various L_2s and αs. As a function of M_t, the natural frequency ratio shows that the tip mass substantially reduces the natural frequency. For instance, a tip-mass ratio of 100% reduces the natural frequency by 73%. In addition, α has a substantial effect than the L_2 effect on the natural frequency sensitivity, indicating that the natural frequency sensitivity for an L_2 range of 5 to 10 mm is less significant. This high tip mass sensitivity suggests that a high tip mass ratio is recommended for considerably lowering the harvester's natural frequency.

Fig. 10 (b) shows the natural frequency ratio as L_2 and α with a fixed tip-mass ratio of 100%. Both L_2 and α have a considerable effect on the natural frequency, yet their effectiveness is not constant. Overall, L_2 causes a more significant natural frequency change than α, and the natural frequency sensitivity diminishes by increasing the L2 and α magnitudes. In other words, the effect of L_2 and α on the natural frequency saturates for great L_2 and α values. This conclusion clarifies the limitation of L_2 and α for natural frequency matching.

Step 3: Structural modulation

The objective function is the difference between the first mode electromechanically coupled resonant frequency and the dominant frequency of car vibration. However, as the resonant frequency of the energy harvester depends on the electrical load, the resonant frequency shift due to the electrical load shall be taken into account [3]. Khazaee et al. [13] investigated the resonant matching considering the electrical load effect, and they recommended setting $\omega_n = \frac{\Omega}{1.04}$ for harmonic analysis. Thus, the objective functions for the three harvester beams can be

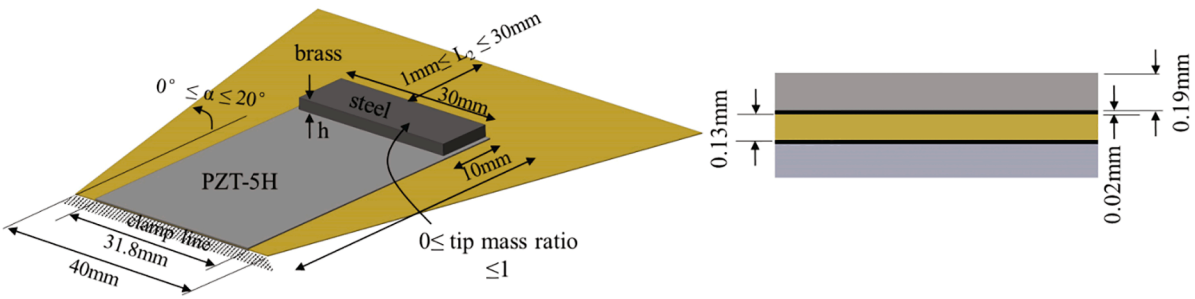

Fig. 8. The optimization benchmark harvester, geometry, and material information.

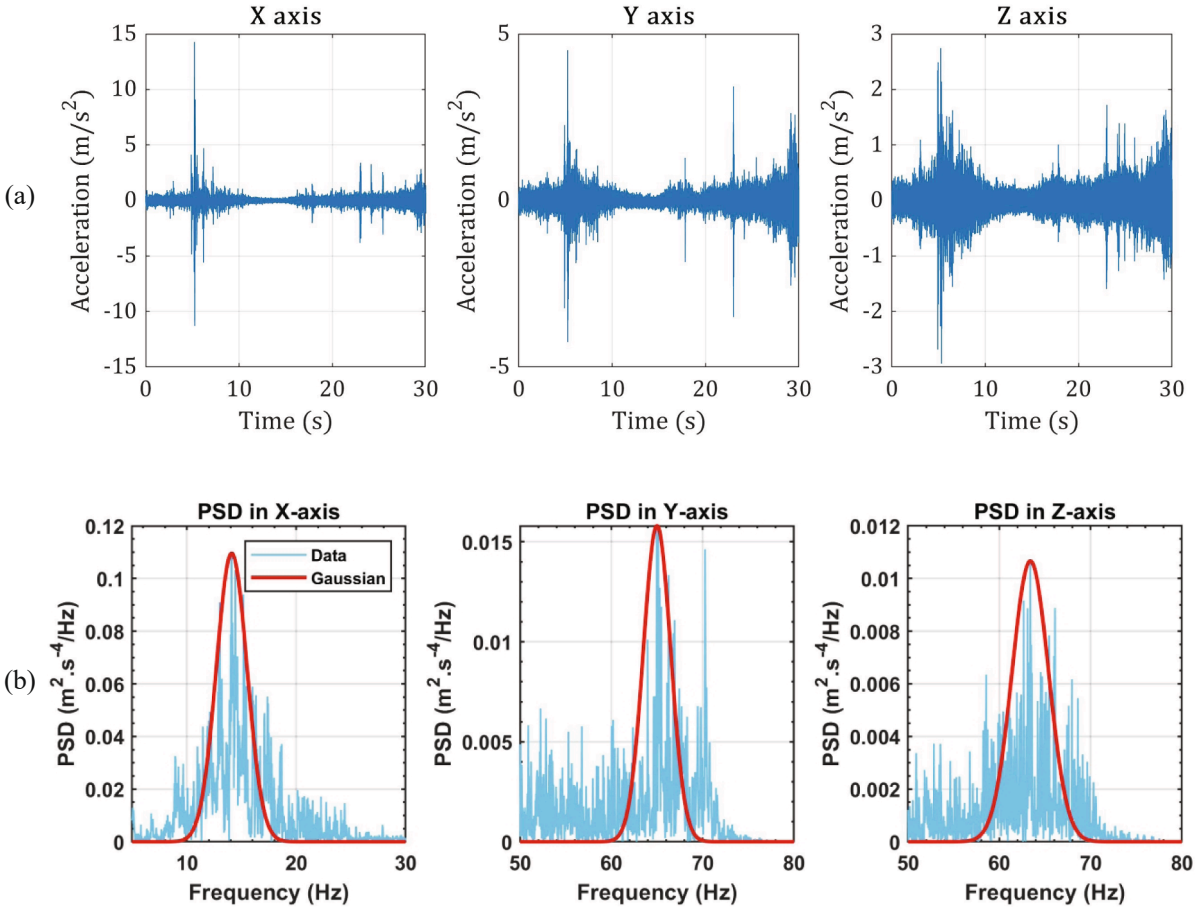

Fig. 9. (a) Time signals and (b) PSD and Gaussian normal distributions of random car vibration in X, Y, and Z axes [45] (x-axis along with the gravity).

expressed with $\epsilon_x(\widehat{\Theta}) = \left(\omega_{\mathrm{n,\,PH_x}} - \frac{\Omega_x}{1.04}\right)^2$, $\epsilon_y(\widehat{\Theta}) = \left(\omega_{\mathrm{n,\,PH_y}} - \frac{\Omega_y}{1.04}\right)^2$ and $\epsilon_z(\widehat{\Theta}) = \left(\omega_{\mathrm{n,\,PH_z}} - \frac{\Omega_z}{1.04}\right)^2$, respectively, where $\widehat{\Theta}$ contains the updating parameters. For reducing the number of updating parameters, α angle is set manually based on the magnitude of the objective frequency. Thus, the independent updating parameters are reduced to L_2 and M_t, i.e., $\widehat{\Theta} = \{L_2, M_t\} \in \mathbb{R}^2$. Since the FE model contains a fine mesh, sensitivity-based optimization is developed to reduce the computation time for the optimization.

- For PH_x harvester:

A tip-mass ratio of 100% is considered, and α is set to −15 in the optimization since the dominant frequency in the X-direction is considerably lower than the reference harvester natural frequency. Note that the tip mass is not constant and varies by beam mass for variable substrate length.

Using the first-order Taylor series approximation, the variation of natural frequency to L_2 can be obtained by:

$$\omega_{\mathrm{n,\,N+1}} \approx \omega_{\mathrm{n,\,N}} + \left.\frac{d\omega_{\mathrm{n,\,N}}}{dL_2}\right|_{\substack{M_t ratio = 100\% \\ \alpha = -15}} \left(L_{2,N+1} - L_{2,N}\right) \tag{14}$$

wherein $\frac{d\omega_{\mathrm{n,\,N}}}{dL_2}$ is the natural frequency sensitivity, previously calculated and shown in Fig. 10 (b).

Using Eq. (7), the updating equation for tuning the length L_2 is given by:

$$L_{2,N+1} \approx L_{2,N} + \frac{\frac{\Omega}{1.04} - \omega_{\mathrm{n,\,N}}}{\left.\frac{d\omega_{\mathrm{n,\,N}}}{dL_2}\right|_{\substack{M_t ratio = 100\% \\ \alpha = -15}}} \tag{15}$$

- For PH_y and PH_z harvester:

The objective frequency is close to the reference bimorph model for these two harvesters. Thus, L_2 and α are set to 0, and the added tip mass is tuned. The equation for updating the tip mass can be obtained similarly, as shown by:

$$M_{t,N+1} \approx M_{t,N} + \frac{\frac{\Omega}{1.04} - \omega_{\mathrm{n,\,N}}}{\left.\frac{d\omega_{\mathrm{n,\,N}}}{dM_t}\right|_{\substack{L_2 = 0 \\ \alpha = 0}}} \tag{16}$$

The optimal parameters from the above sensitivity-based method are given in Table 4. The optimal parameters are obtained after four iterations, a low iteration number. As shown in Table 4, the optimized natural frequency is satisfactorily close to the objective frequency demonstrating the reported optimization's convergence ability for frequency matching.

Step 4: Electrical modulation

After geometry optimizations, the optimum electrical load should be selected to have the maximum power. Two approaches can be taken. One, which is the standard practice in VPEH, is to find the optimum load under the resonant excitation analysis. The other is to compute the output power based on the entirely random vibration analysis. For the

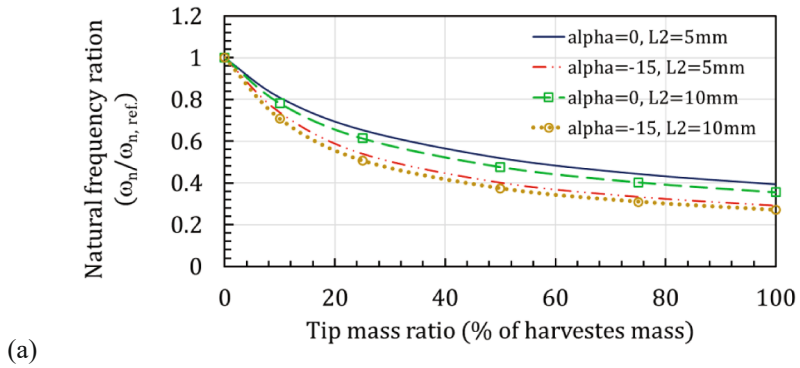

(a)

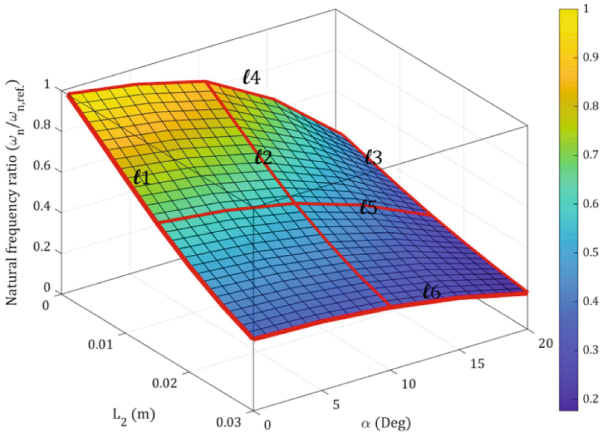

			$\Delta\omega_n/\omega_{n,\text{ref.}}$
ℓ1	α=0°	Variable L_2	0.75
ℓ2	Mid α	Variable L_2	0.56
ℓ3	high α	Variable L_2	0.22
ℓ4	Variable α	Low L_2	0.60
ℓ5	Variable α	Mid L_2	0.37
ℓ6	Variable α	High L_2	0.18

(b)

Fig. 10. The sensitivity of fundamental natural frequency as a function of (a) tip-mass and (b) substrate excess length and tapering angle with tip-mass ratio 100%.

Table 4
Optimized parameters of the harvester's substrate and tip mass for the resonant frequency matching.

		PH_x	PH_y	PH_z
Objective frequency (=Ω/1.04)		13.56	62.50	60.96
Natural frequency after optimization process		13.57	62.90	60.84
Optimized substrate characteristics	L_2 (mm)	12.9	0	0
	α (deg)	−15	0	0
	M_t (gr)	11.9	1.1	1.3

harmonic analysis, an input acceleration of unit gravity, g = 9.81 m/s^2, is considered under harmonic excitation, e.g., $\ddot{a}_B(t) = g\sin(\omega_{n,\text{opt}}t)$, and the output power is calculated over different load conditions for the case of optimized length. Two frequency excitations are considered, namely $\omega = \omega_n$ similar to common practice in the literature, and $\omega = 1.04\omega_n$, as suggested by [13]. The numerical integration calculates the output power over the total frequency range for the random analysis. Therefore, it is expected that the random analysis is the most accurate.

Fig. 11 shows the output power as a function of electrical loads for the harmonic and random analyses. The optimum load with harmonic analysis under $\omega = 1.04\omega_n$ is 22 kΩ and under $\omega = \omega_n$ is 15 kΩ, while the optimum load by the random vibration analysis is 29 kΩ. The harmonic analysis underestimates the optimum load for this actual car excitation. Therefore, a random analysis is required for real-time vibration sources. This result agrees with the random analysis study by Halvorsen [14], where they argued that the optimum load between the wideband random signal is different from the harmonic signal. However, the optimum load from harmonic excitation with $\omega = 1.04\omega_n$ frequency is closer to the actual value. Therefore, Ref. [13] 's suggestion, derived

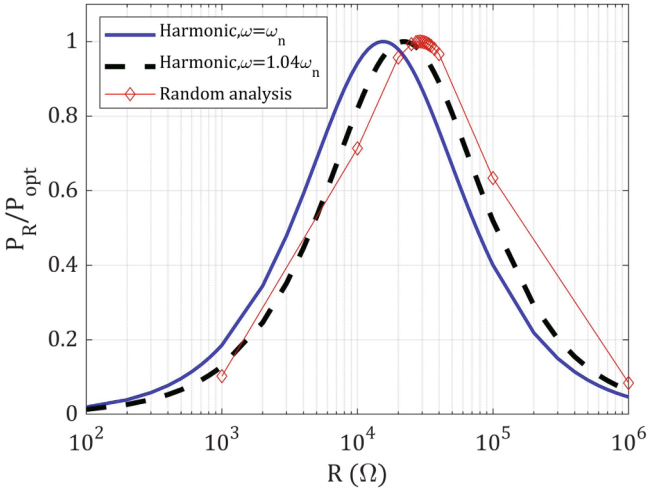

Fig. 11. Optimum electrical load for the PH_x harvester from harmonic and random excitation analyses.

from the harmonic excitations, gives a better result than random excitation.

As discussed in subsection 2.1, the optimum load depends on the material properties, geometrical parameters, and excitation frequency. The frequency dependency is often hidden yet vital because this is an external factor in the harvester system design. The optimum load depends considerably on the excitation frequency, as seen from Fig. 12 from the numerical FE solutions. At the maximum power generation, e.

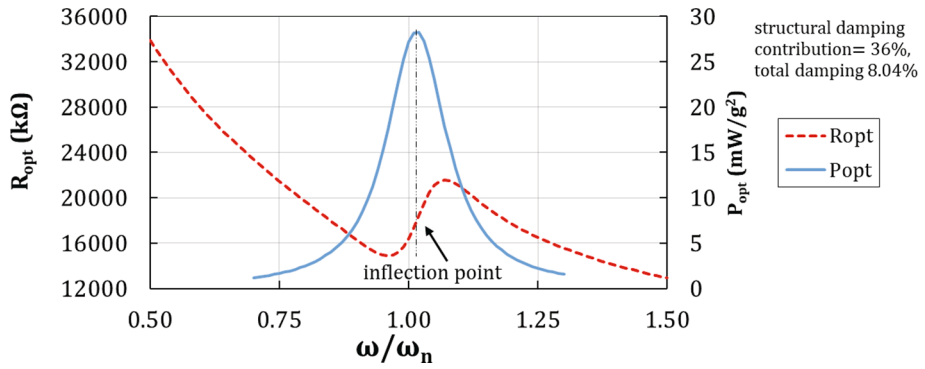

Fig. 12. Optimum load and optimum power with the excitation frequency for the optimized PH_x harvester.

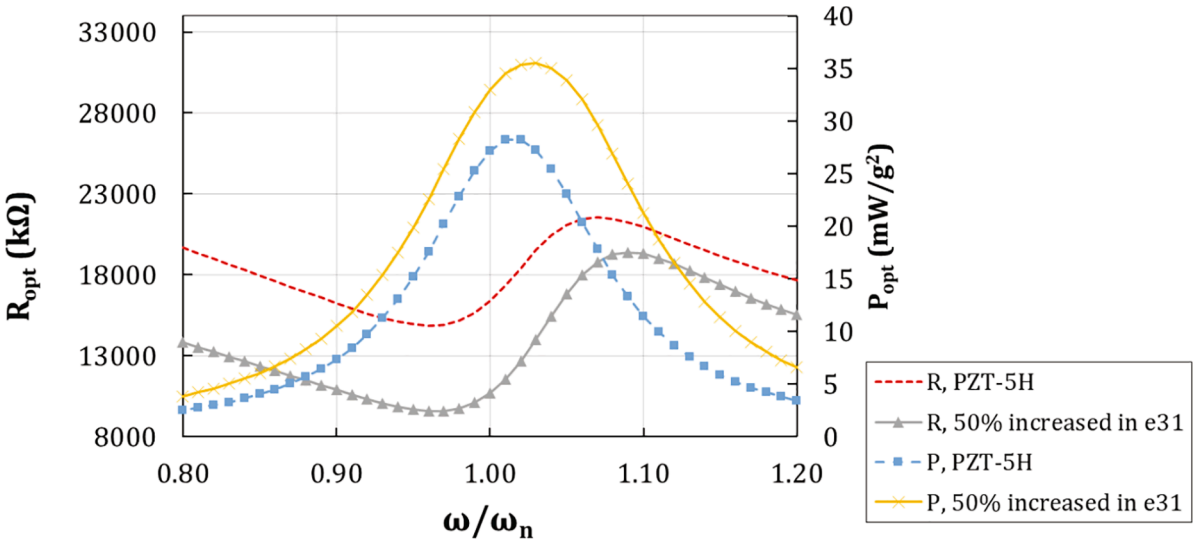

Fig. 13. The effect of piezoelectric conversion coefficients on the frequency dependency of optimum load and optimum power (when the piezoelectric coupling coefficients are increased by 50%).

g., $\omega/\omega_n \approx 1.03$, there is an inflection point in the optimum load graph. For $0.9 < \omega/\omega_n < 1.1$, the optimum load is specially highly sensitive to the excitation frequency. At low-frequency excitation, such as $\omega/\omega_n < 0.75$, when the dynamic effect becomes less significant, the optimum load rises sharply, reaching approximately $R_{opt} = 129$ kΩ for $\omega/\omega_n = 0.1$. On the other hand, the optimum load considerably reduces for the high frequency excitation. For instance, R_{opt} is 1.5 kΩ for $\omega/\omega_n = 10$.

The inflection point and extremum points in the optimum resistance curve are expected to depend on the piezoelectric coupling coefficients, same as the resonant frequencies of the harvester [46]. For exploring the piezoelectric coefficient effect, the optimum load and power are again calculated for a hypothetical material with a 50% increase in its piezoelectric coefficient, as depicted in Fig. 13. When the piezoelectric conversion coefficients increase, the inflection point shifts to the right, proving the link between the conversion coefficient and inflection point. Here, only a brief investigation of the optimum load is presented, but a detailed study is recommended for the optimum load analysis due to many controlling material and geometrical parameters.

Table 5
The output voltage and power from optimized piezoelectric harvesters using random excitation analysis.

Optimized substrate characteristics	PH_x	PH_y	PH_z
The optimum load from random input analysis	29,000		
The optimum average voltage, E[V(t)] (V)	13.60	3.42	3.00
The optimum average power, E[P(t)] (mW)	1.32	0.11	0.09
The optimum average power density (μW/cm³)	425.92	80.80	64.88

Discussion on power generation estimation

After geometry optimizations and optimum electrical load selection, the output power from the stochastic vibration can be derived from Eq. (7) by numerical integration over the frequency range, performed by the trapezoid integration method.

As a case study, the stochastic vibration from one typical input signal from Fig. 9 is considered for demonstrating the optimized harvester. A three-axis stochastic acceleration was used in Fig. 8, and harvesters associated with different directional excitations called PH_x, PH_y, and PH_z (See Fig. 1). Table 5 shows the optimized output voltage and power from the PH_x, PH_y, and PH_z harvesters. As shown in Table 5, the gravity-excitation harvester, X-axis, generates the highest power output, an average power of 1.32 mW. The power density values at different axes are also shown in Table 5. The X-axis harvester generates a power density of 425 μW/cm^3, which is considerably higher than the others are. This higher power generation is expected, as the tip mass and input vibration level for the PH_x harvester is more significant than for other harvesters because the car vibration from a straight path is considered in this study. If setting-off, turning, and braking maneuvers are simulated [33], PH_y and PH_z harvesters are expected to generate more power. Nevertheless, these maneuvers require a comprehensive and separate study out of the current paper's scope.

The average power output, defined by Eq. (7), e.g., $E[P(t)] = \frac{1}{R}\left(\int_{-\infty}^{\infty} \overbrace{|H(\omega)|^2 \Phi_{BB}(\omega)}^{\Phi_{VV}(\omega)}\right)$, is the integration of the product of $|H(\omega)|$, the

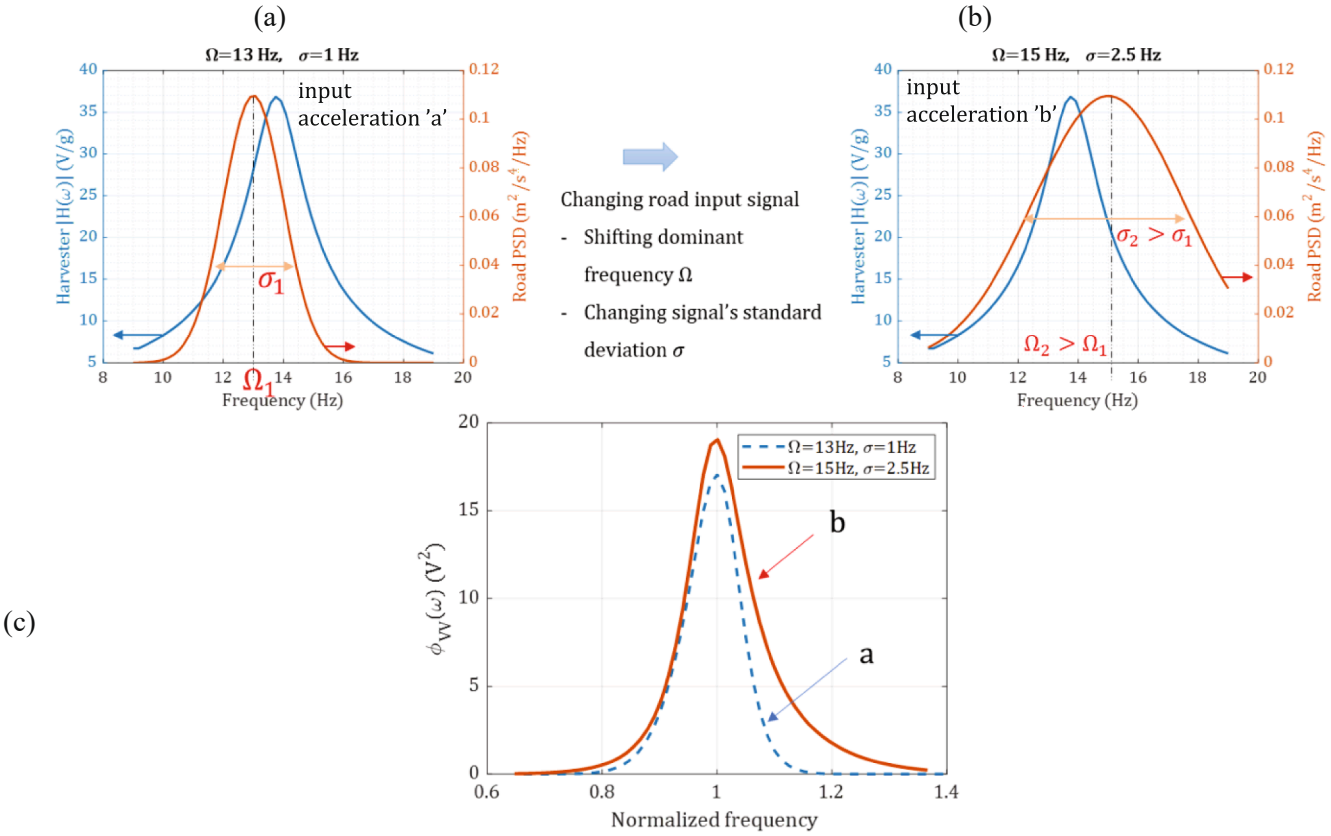

Fig. 14. Presenting the effect of stochastic input acceleration characteristics on the piezoelectric output voltage power spectrum, (a) the input acceleration type '*a*', (b) the input acceleration type '*b*' and (c) the output voltage comparisons between input signals '*a*' and '*b*'.

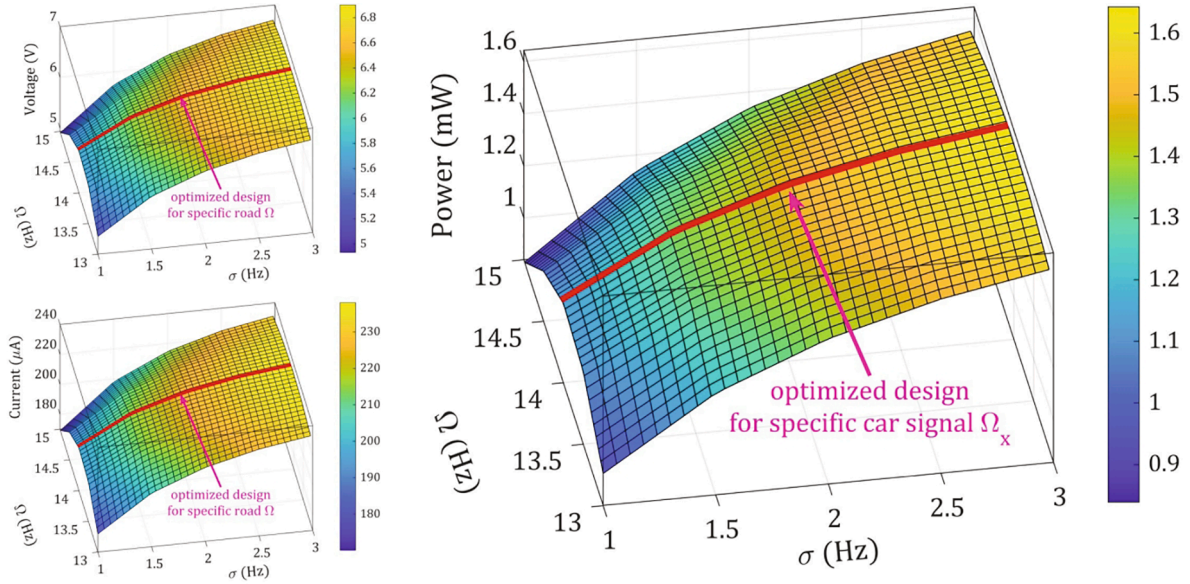

Fig. 15. Effect of input stochastic vibration characteristics, the dominant frequency Ω, and bandwidth σ, on the output voltage, current, and power.

harvester's transfer function, and $\Phi_{BB}(\omega)$, the input vibration power spectral density. Thus, the peaks of $|H(\omega)|_{\max}$ and $(\Phi_{BB}(\omega))_{\max}$, the bandwidth σ, and the dominant peak's location in the frequency axis Ω, are significant. The whole subsection 2.2, design of piezoelectric harvesting device, focused on the harvester transfer function $|H(\omega)|$, and its optimization while stochastic source dependency has not been thoroughly studied. For demonstrating the stochastic source importance, two input acceleration signals, '*a*' and '*b*' with $\sigma_2 > \sigma_1$ and $\Omega_2 > \Omega_1$, are shown in Fig. 14 (a) and (b), respectively. The voltage power spectral density for these two acceleration signals is compared in Fig. 14 (c), which clearly shows that the output voltage spectrum differs. This comparison demonstrates how the piezoelectric voltage varies by the stochastic input signal for a system transfer function.

Further sensitivity analysis of piezoelectric PH_x performance with

the input stochastic acceleration is demonstrated in Fig. 15. The stochastic acceleration variables are the dominant frequency 13 Hz $< \Omega <$ 15 Hz and the acceleration bandwidth 1 Hz $< \sigma <$ 3 Hz. The following remarks can be made:

- Higher stochastic vibration bandwidth σ leads to higher power generation because of wideband input excitation. The sensitivity to wide bandwidth becomes less important at extremely high σ, since the voltage transfer function $|H(\omega)|$ is also a narrowband function.
- The power is maximum for the modulated dominant frequency Ω_x, and the power reduces either for smaller or for greater dominant frequencies. The dominant frequency sensitivity is more substantial for narrowband stochastic signal, e.g., smaller σ, and flatter for wideband input stochastic vibration.

From an energy harvesting perspective, the voltage, current, and power output for the modulated energy harvester in a Gaussian stochastic input acceleration with 0.109 $m^2. s^{-4}$/Hz peak amplitude, dominant frequency 13 Hz $< \Omega <$ 15 Hz, and acceleration bandwidth 1 Hz $< \sigma <$ 3 Hz are between 5 and 7 V, 160 to 240 μA, and 0.8 to 1.32 mW. This power output is estimated from the stochastic car vibration of a moving car on an urban road [45]. The power output has linear variation concerning the input acceleration stochastic PSD, and therefore for different input signal magnitudes, the power can be estimated. The measured car stochastic vibration at the highway and urban road lies within $\sim <$ 0.05 $m^2. s^{-4}$/Hz and $\sim >$ 0.08 $m^2. s^{-4}$/Hz [45], thus the power of $<$ 0.6 mW is expected on the highway and $>$ 1.0 mW for the urban road.

Conclusion and future work

A study was presented about designing an energy-harvesting device with piezoelectric harvesters to generate energy from car vibration. An experimentally validated finite element model is developed for the random base vibration. Then, the design and optimization of a non-uniform piezoelectric harvester are carried out. First, car vibration signals were analyzed, and their characteristics were used for the geometric design of piezoelectric beams. Later, a sensitivity-based optimization process was carried out for selecting the optimum load resistance. Finally, the output power was calculated using the developed model for the piezoelectric harvester. The following remarks can be made from this study:

- A finite element model is developed for analyzing piezoelectric harvester's performance under random base vibration.
- The finite element model can accurately model the structural response considering the contact layer.
- A combined viscous-structural damping model is essential for proper power output estimation.
- The sensitivity-based optimization process can reliably and quickly be employed for resonant-matching designs.
- Optimum load resistance for maximum power generation under natural vibration shall be investigated considering the random vibration analysis.
- The optimal energy harvester has a power of 1.32 mW and a power density of 425.92 μW/cm^3.

Required power consumption for truly wireless sensors is previously reported. A fully autonomous wireless vibration sensor (WVS) consumes energy of 360 μJ during one 3.28 s-duration cycle [47], comprising a 20.8 ms-duration acceleration measurement, a 4.5 ms-duration radio frequency data transmission, and the rest is sleeping mode. Thus, the power required for a wireless sensor is 109.76 μW. Other studies for WNS power estimation are 900 μW at a 10 Hz update rate [48], the average power of 400 to 600 μW [49], and the RF CMOS transmitter with 300 μW power from a 1-V supply [50]. The optimal energy harvester generates 425.92 μW/cm^3; according to Table 5, the energy harvester PH_x can provide the power required for the autonomous WVS. Therefore, the designed energy harvester can be attached to the car's frame, and it can feed power to the autonomous WVS. However, the electrical current generation is approximately 200 μA, which is lower than the required for electronic consumption, suggesting the use of multiple harvesters and the DC-DC converter.

Future works include practical demonstration, conversion efficiency improvement, and field testing to propose piezoelectric-based wireless sensors. In addition, various locations in the car shall be investigated to provide an "Energy Generation Contour." Toward conversion efficiency improvement, a detailed analysis of the optimum load and its dependency on various material properties and geometrical parameters is suggested. The practical demonstration shall consider power management circuits, power storage, and converters. As vital issues, the issues with a cold start, electronic loss, and low current generation need microelectronic knowledge, which shall be included in future works. The narrowband issue for useful stochastic vibration sources needs further research by changing the car's working condition (engine rotation speed). Adding nonlinear boundary conditions, such as variable span stopper and hybrid magnetic forces. Material efficiency improvement ensures enough power generation at very-low amplitude vibration. Some possible future configuration focuses are optimum beam geometry, composite Piezoceramic fiber with optimal fiber orientation, and variable thickness. Addressing these research questions opens a robust candidate application in smart cars for piezoelectric harvesters.

CRediT authorship contribution statement

Majid Khazaee: Conceptualization, Methodology, Writing – original draft, Software, Data curation, Visualization. **Alireza Rezania:** Methodology, Investigation, Supervision. **Lasse Rosendahl:** Methodology, Supervision.

Declaration of Competing Interest

The authors declare that they have no known competing financial interests or personal relationships that could have appeared to influence the work reported in this paper.

Appendix A. Supplementary data

Supplementary data to this article can be found online at https://doi.org/10.1016/j.seta.2022.102228.

References

[1] Zhang J, Yu X, Zhao W, Qu D. A piezoelectric vibration energy harvester based on the reverse-rhombus double-bridge force amplification frame. J Phys D: Appl Phys 2021;54(36):365501.
[2] Lim D-W, Mantell SC, Seiler PJ. Wireless monitoring algorithm for wind turbine blades using Piezo-electric energy harvesters. Wind Energy 2017;20(3):551–65. https://doi.org/10.1002/we.
[3] Khazaee M, Rezaniakolaie A, Moosavian A, Rosendahl L. A novel method for autonomous remote condition monitoring of rotating machines using piezoelectric energy harvesting approach. Sensors Actuators A Phys 2019;295:37–50. https://doi.org/10.1016/j.sna.2019.05.016.
[4] Wischke M, Masur M, Kröner M, Woias P. Vibration harvesting in traffic tunnels to power wireless sensor nodes. Smart Mater Struct 2011;20(8):085014.
[5] Roshani H, Dessouky S, Montoya A, Papagiannakis AT. Energy harvesting from asphalt pavement roadways vehicle-induced stresses: A feasibility study. Appl Energy 2016;182:210–8. https://doi.org/10.1016/j.apenergy.2016.08.116.
[6] Khazaee M, Rezaniakolaei A, Rosendahl L. An experimental study on macro piezoceramic fiber composites for energy harvesting. Mater Sci Forum 2019;vol. 951 MSF:3–8. https://doi.org/10.4028/www.scientific.net/MSF.951.3.
[7] Cao Y, Huang H, Ding Y. Isogeometric optimization of piezoelectric functionally graded material for energy harvester. Compos Struct 2021;vol. 273, no. March: 114261. https://doi.org/10.1016/j.compstruct.2021.114261.
[8] T. Wang and Z. W. Zhu, "A new type of piezoelectric self-excited vibration energy harvester for micro-actuator's energy storage," *J. Energy Storage*, vol. 46, no. December 2021, p. 103519, 2022, doi: 10.1016/j.est.2021.103519.

[9] A. R. G. da Silveira and G. B. Daniel, "Optimization analysis of an energy harvester for smart tilting pad journal bearings considering higher vibration modes," *Mech. Syst. Signal Process.*, vol. 166, no. March 2021, pp. 1–18, 2022, doi: 10.1016/j.ymssp.2021.108404.
[10] Y. Ma, J. Wang, C. Li, and X. Fu, "A micro-power generator based on two piezoelectric MFC films," *Crystals*, vol. 11, no. 8, 2021, doi: 10.3390/cryst11080861.
[11] Fan Y, Ghayesh MH, Lu T-F, Amabili M. Design, development, and theoretical and experimental tests of a nonlinear energy harvester via piezoelectric arrays and motion limiters. Int J Non Linear Mech 2022;142:103974. https://doi.org/10.1016/j.ijnonlinmec.2022.103974.
[12] A. Calderon Hurtado, P. Peralta, R. O. Ruiz, M. Makki Alamdari, and E. Atroshchenko, "Shape optimization of piezoelectric energy harvesters of variable thickness," *J. Sound Vib.*, vol. 517, no. September 2021, p. 116503, 2022, doi: 10.1016/j.jsv.2021.116503.
[13] M. Khazaee, A. Rezania, and L. Rosendahl, "An experimental study to determine damping of piezoelectric harvesters using transient analysis of unified electromechanical voltage equation," *Energy Convers. Manag.*, vol. 227, no. July 2020, p. 113567, 2021, doi: 10.1016/j.enconman.2020.113567.
[14] Halvorsen E. Energy harvesters driven by broadband random vibrations. J Microelectromechanical Syst 2008;17(5):1061–71. https://doi.org/10.1109/JMEMS.2008.928709.
[15] Lefeuvre E, Badel A, Richard C, Guyomar D. Energy harvesting using piezoelectric materials: Case of random vibrations. J Electroceramics 2007;19(4):349–55. https://doi.org/10.1007/s10832-007-9051-4.
[16] Blystad LCJ, Halvorsen E, Husa S. Piezoelectric MEMS energy harvesting systems driven by harmonic and random vibrations. IEEE Trans Ultrason Ferroelectr Freq Control 2010;57(4):908–19. https://doi.org/10.1109/TUFFC.2010.1495.
[17] Adhikari S, Friswell MI, Inman DJ. Piezoelectric energy harvesting from broadband random vibrations. Smart Mater Struct 2009;18(11):115005.
[18] Zhang Y, Jiao Z, Duan X, Xu Y. Stochastic dynamics of a piezoelectric energy harvester with fractional damping under Gaussian colored noise excitation. Appl Math Model 2021;97:268–80. https://doi.org/10.1016/j.apm.2021.03.032.
[19] Renaud M, Elfrink R, Jambunathan M, de Nooijer C, Wang Z, Rovers M, et al. Optimum power and efficiency of piezoelectric vibration energy harvesters with sinusoidal and random vibrations. J Micromech Microeng 2012;22(10):105030.
[20] Yoon H, Kim M, Park C-S, Youn BD. Time-varying output performances of piezoelectric vibration energy harvesting under nonstationary random vibrations. Smart Mater Struct 2018;27(1):015004.
[21] Yang F, Gao M, Wang P, Zuo J, Dai J, Cong J. Efficient piezoelectric harvester for random broadband vibration of rail. Energy Mar. 2021;218:119559. https://doi.org/10.1016/J.ENERGY.2020.119559.
[22] Xie XD, Wang Q. Energy harvesting from a vehicle suspension system. Energy 2015;86:382–95. https://doi.org/10.1016/j.energy.2015.04.009.
[23] Maurya D, Kumar P, Khaleghian S, Sriramdas R, Kang MG, Kishore RA, et al. Energy harvesting and strain sensing in smart tire for next generation autonomous vehicles. Appl Energy 2018;232:312–22.
[24] Morangueira YLA, de C. Pereira JC. Energy harvesting assessment with a coupled full car and piezoelectric model. Energy 2020;210:1–13. https://doi.org/10.1016/j.energy.2020.118668.
[25] M. Khazaee, A. Rezaniakolaei, and L. Rosendahl, "A comprehensive electromechanically coupled model for non-uniform piezoelectric energy harvesting composite laminates," *Mech. Syst. Signal Process.*, vol. 145, no. November-December, p. 106927, 2020.
[26] Khazaee M, Huber JE, Rosendahl L, Rezania A. On the determination of viscous and structural damping coefficients for piezoelectric energy harvesters using only time-domain voltage measurements. Appl Energy 2021;285:116427.
[27] Piliposian G, Hasanyan A, Piliposyan G, Jilavyan H. The effect of the location of piezoelectric patches on the sensing, actuating and energy harvesting properties of a composite plate with piezoelectric patches. Int J Precis Eng Manuf - Green Technol 2020;7(3):657–68. https://doi.org/10.1007/s40684-020-00219-1.
[28] Zou H-X, et al. Mechanical modulations for enhancing energy harvesting: Principles, methods and applications. Appl Energy 2019;255:113871.
[29] H. Masoumi, H. Moeenfard, H. H. Khodaparast, and M. I. Friswell, "On the effects of structural coupling on piezoelectric energy harvesting systems subject to random base excitation," *Aerospace*, vol. 7, no. 7, 2020, doi: 10.3390/AEROSPACE7070093.
[30] S. Hu, S. Bouhedma, A. Schütz, S. Stindt, D. Hohlfeld, and T. Bechtold, "Design optimization of multi-resonant piezoelectric energy harvesters," *Microelectron. Reliab.*, vol. 120, no. December 2020, p. 114114, 2021, doi: 10.1016/j.microrel.2021.114114.
[31] Jo K, Kim J, Kim D, Jang C, Sunwoo M. Development of autonomous car-part i: Distributed system architecture and development process. IEEE Trans Ind Electron 2014;61(12):7131–40. https://doi.org/10.1109/TIE.2014.2321342.
[32] M. Gholikhani, H. Roshani, S. Dessouky, and A. T. Papagiannakis, "A critical review of roadway energy harvesting technologies," *Appl. Energy*, vol. 261, no. July 2019, p. 114388, 2020, doi: 10.1016/j.apenergy.2019.114388.
[33] Rui X, Li Y, Zheng X, Sha Z, Zeng Z. Design and experimental study of a piezoelectric energy harvester in automotive spokes. J Phys D: Appl Phys 2019;52(35):355501.
[34] He J, Fu Z-F. Modal analysis. 1st ed. Butterworth-Heinemann; 2001.
[35] Piezo.com, "Products Datasheet & User Manual," 2021. https://piezo.com/collections/piezoelectric-actuators-motors/products/piezoelectric-bending-transducer-q220-h4br-2513yb (accessed Jul. 23, 2021).
[36] Khazaee M, Rezaniakolaei A, Rosendahl L. A proof for looking differently into damping modeling in piezoelectric energy harvesting systems. In: in *Proceedings of the 26th International Congress on Sound and Vibration*; 2019, 2019,. p. 1–8.
[37] Khazaee M, Rezania A, Rosendahl L. Effect of damage and support damping mechanisms on unimorph piezoelectric energy harvester. J Vib Control 2019;25(18):2409–22.
[38] Banks HT, Inman DJ. On damping mechanisms in beams. J Appl Mech Trans ASME 1991;58(3):716–23. https://doi.org/10.1115/1.2897253.
[39] Hosaka H, Itao K, Kuroda S. Damping characteristics of beam shaped micro oscillators. Sensors Actuators A Phys 1995;49(1–2):57–95.
[40] Cooley CG, Tran TQ, Chai T. Comparison of viscous and structural damping models for piezoelectric vibration energy harvesters. Mech Syst Signal Process 2018;110:130–8. https://doi.org/10.1016/j.ymssp.2018.03.017.
[41] Chi Z, He Y, Naterer GF. Design optimization of vehicle suspensions with a quarter-vehicle model. Trans Can Soc Mech Eng 2008;32(2):297–312.
[42] D.E.Newland, *An introduction to random vibrations and spectral analysis*, 3rd ed. Longman Scientific & Technical, 1993.
[43] Seyranian AP, Lund E, Olhoff N. Multiple eigenvalues in structural optimization problems. Struct Optim 1994;8(4):207–27. https://doi.org/10.1007/BF01742705.
[44] Lopes MV, Eckert JJ, Martins TS, Santos AA. Optimization of EH multi-beam structures for freight car vibration. IFAC-PapersOnLine 2018;51(2):849–54. https://doi.org/10.1016/j.ifacol.2018.04.020.
[45] Neri I, Travasso F, Mincigrucci R, Vocca H, Orfei F, Gammaitoni L. A real vibration database for kinetic energy harvesting application. J Intell Mater Syst Struct 2012;23(18):2095–101. https://doi.org/10.1177/1045389X12444488.
[46] DuToit NE, Wardle BL, Kim SG. Design considerations for MEMS-scale piezoelectric mechanical vibration energy harvesters. Integr Ferroelectr 2005;71:121–60. https://doi.org/10.1080/10584580590964574.
[47] Torah RN, Tudor MJ, Patel K, Garcia IN, Beeby SP. Autonomous low power microsystem powered by vibration energy harvesting. Proc IEEE Sensors 2007:264–7. https://doi.org/10.1109/ICSENS.2007.4388387.
[48] Owen TH, Kestermann S, Torah R, Beeby SP. Self powered wireless sensors for condition monitoring applications. Sens Rev 2009;29(1):38–43. https://doi.org/10.1108/02602280910926742.
[49] Roundy S, Leland ES, Baker J, Carleton E, Reilly E, Lai E, et al. Improving power output for vibration-based energy scavengers. IEEE Pervasive Comput 2005;4(1):28–36.
[50] Otis BP, Rabaey JM. A 300μmW 1.9GHz CMOS oscillator utilizing micromachined resonators. Eur Solid-State Circuits Conf 2002;38(7):151–4.